nature nanotechnology

Article

https://doi.org/10.1038/s41565-023-01521-0

Optical gain and lasing from bulk cadmium sulfide nanocrystals through bandgap renormalization

Received: 6 February 2023

Accepted: 6 September 2023

Published online: 05 October 2023

Check for updates

Ivo Tanghe[1,2,3], Margarita Samoli[3], Isabella Wagner[4,5], Servet Ataberk Cayan[2,3], Ali Hossain Khan[6,9], Kai Chen[5,7,8], Justin Hodgkiss[4,5], Iwan Moreels[3], Dries Van Thourhout[1,2], Zeger Hens[2,3] & Pieter Geiregat[2,3]

Strongly confined colloidal quantum dots have been investigated for low-cost light emission and lasing for nearly two decades. However, known materials struggle to combine technologically relevant metrics of low-threshold and long inverted-state lifetime with a material gain coefficient fit to match cavity losses, particularly under electrical excitation. Here we show that bulk nanocrystals of CdS combine an exceptionally large material gain of 50,000 cm^{-1} with best-in-class gain thresholds below a single exciton per nanocrystal and 3 ns gain lifetimes not limited by non-radiative Auger processes. We quantitatively account for these findings by invoking a strong bandgap renormalization effect, unobserved in nanocrystals to date, to the best of our knowledge. Next, we demonstrate broadband amplified spontaneous emission and lasing under quasi-continuous-wave conditions. Our results highlight the prospects of bulk nanocrystals for lasing from solution-processable materials.

Optoelectronics based on solution-processable materials, such as small-molecule organics[1] or strongly confined colloidal quantum dots (QDs)[2–4], holds great promise for low-cost, flexible optoelectronic devices. Over the past 20 years, such promise was indeed met in the fields of light-emitting diodes for lighting and displays[5], photovoltaics[6] and photodetection[7–9]. In such applications, excitation densities far below a single exciton per QD on average are used, and the interaction with light is dictated by linear absorption and spontaneous emission. Pushing these materials to a net optical gain—a regime of high excitation density where stimulated emission overtakes both absorption and spontaneous emission—remains, however, a huge challenge as of today. Inorganic nanocrystals are probably the most promising candidates to achieve stable room-temperature lasing due to a unique combination of a long-term structural stability and an electronic structure tunable by size, shape and composition[2,3]. After two decades of research[10], a broad scope of optical gain mechanisms have been investigated. All of these approaches share the common element that at least one spatial dimension of the QD is under strong quantum confinement. To understand the limitations of these confined QDs as a gain material, three gain metrics are used for benchmarking: the inverted-state (or 'gain') lifetime τ_G, the threshold carrier density n_{th} and the material gain coefficient g_i. Although the lifetime and threshold (density) determine the lasing pump threshold $J_{th} \propto n_{th}/\tau_G$ under electrical or continuous-wave (CW) optical excitation,

[1]Photonics Research Group, Ghent University, Gent, Belgium. [2]NoLIMITS Center For Non-Linear Microscopy and Spectroscopy, Ghent University, Gent, Belgium. [3]Physics and Chemistry of Nanostructures, Ghent University, Gent, Belgium. [4]School of Chemical and Physical Sciences, Victoria University of Wellington, Wellington, New Zealand. [5]MacDiarmid Institute for Advanced Materials and Nanotechnology, Wellington, New Zealand. [6]Department of Chemical and Biological Sciences, S. N. Bose National Centre for Basic Sciences, Kolkata, India. [7]Robinson Research Institute, Victoria University of Wellington, Wellington, New Zealand. [8]The Dodd-Walls Centre for Photonic and Quantum Technologies, University of Otago, Dunedin, New Zealand. [9]Present address: Ghent University, Physics and Chemistry of Nanostructures, Gent, Belgium. e-mail: pieter.geiregat@ugent.be

https://doi.org/10.1038/s41565-023-01521-0

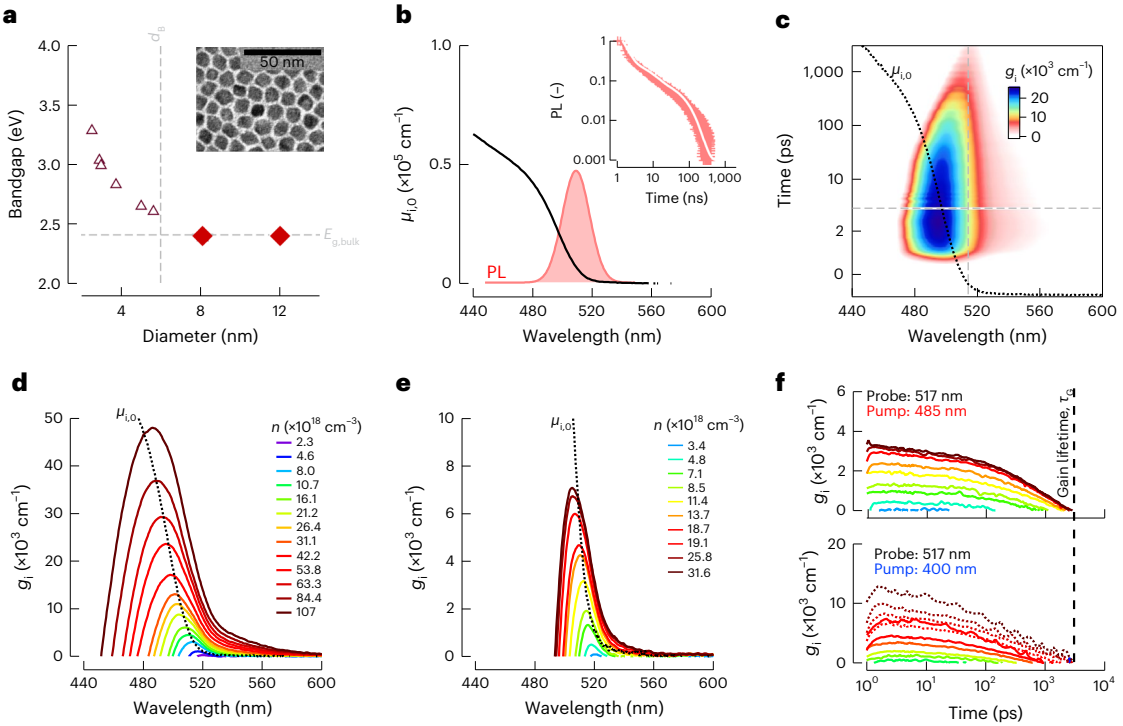

Fig. 1 | Photophysical properties of CdS BNCs. a, Sizing curve of wz–CdS (empty triangles) combined with the bandgap energy/size pairs (red diamonds) for our bulk-like CdS BNCs[30]. The vertical dashed line indicates the Bohr diameter (5.6 nm) and the horizontal dashed line shows the bulk bandgap of wz–CdS (2.398 eV; 517 nm). The inset shows a TEM image of the 12.0 ± 2.0 nm (mean) CdS BNCs. **b**, Linear absorption (black), represented as the intrinsic absorption coefficient $\mu_{i,0}$, and the spontaneous PL after 400 nm excitation. The inset shows the integrated PL decay (red) fitted with a triple-exponential function (white line). **c**, False-colour map of the material gain $g_i(\lambda, t) > 0$ after photoexcitation with 400 nm, creating a carrier density of $n = 5.4 \times 10^{19}$ cm^{-3}. The dotted black line indicates the linear intrinsic absorption spectrum $\mu_{i,0}$. The dashed lines indicate the spectral position (517 nm) and time (3 ps) where slicing is performed for **d**–**f**. **d**,**e**, Material gain spectra $g_i(\lambda)$ at 3 ps time delay for pumping at 400 nm (**d**) and 485 nm (**e**), for increasing carrier density n. **f**, Dynamics of the material gain $g_i(t)$ at the bandgap (517 nm) after photoexcitation with 400 nm (top graph) and 485 nm (bottom graph) for similar carrier densities as those in **d** and **e**. The vertical dashed line indicates the gain lifetime τ_G, reaching up to 3 ns for both pumping conditions.

the often overlooked g_i dictates whether losses of a laser cavity can be compensated.

Champions in each metric have been reported, including type-II QDs[11–14] and electron-doped systems, with record low n_{th} but limited g_i; two-dimensional nanoplatelets[15–18], with record g_i but sub-nanosecond τ_G; and CdSe/CdS QDs that offer a compromise solution on three fronts, mainly driven by small biexciton redshifts of less than 10 meV (Supplementary Table 4)[19]. Several breakthroughs were made nonetheless in recent years leading to a single report on CW optically pumped lasing and numerous attempts at electrically excited stimulated emission[20–27]. It has become clear that both CW optical and d.c. electrical excitation drive up the losses of the photonic cavity that push the required material gain to levels not reachable by current state-of-art CdSe/CdS architectures[19].

Here we show that CdS nanocrystals with sizes exceeding the upper limit for strong quantization provide the desired combination of optimized gain metrics in a single material. These so-called bulk nanocrystals (BNCs) provide gain values up to 50,000 cm^{-1}, sub-single-exciton gain thresholds and a 3 ns gain lifetime uniquely limited by a radiative recombination process. Building on these metrics, we show highly efficient amplified spontaneous emission (ASE) in thin films, enabling a series of optically pumped lasers across the blue/green spectrum under quasi-CW operation.

Optical gain with BNCs

For this work, a series of CdS nanocrystals with wurtzite (wz) crystal structure and sizes varying from 8 to 12 nm were synthesized using a continuous-injection procedure (Methods and Supplementary Section 1). Hereafter, we focus on the 12 nm size, unless mentioned otherwise. In Fig. 1a (inset), a transmission electron microscopy (TEM) image of the monodisperse particles with an average size of 12 ± 2 nm is shown. In Fig. 1b, the normalized absorption spectrum $\mu_{i,0}(\lambda)$ (ref. 28) is shown together with the photoluminescence (PL) spectrum. The PL quantum yield is determined as 15% and the inset in Fig. 1b shows the PL decay fitted to a triple exponential, where the fastest component has a decay rate $k_1 = 0.33$ ns^{-1} ($\tau_1 = 3.0$ ns), tentatively assigned to trapping processes (Supplementary Section 1.2)[29]. Figure 1a shows the wz–CdS sizing curve together with the samples used here[30]. Beyond the Bohr diameter[31], we observe a flat dispersion levelling off at the bulk gap, indicating that our particles are no longer subject to quantum confinement. Such assignments are in line with a recent report that puts a limit on confinement for CdS at 6.3 nm (ref. 32). We, therefore, label the particles as BNCs (bulk nanocrystals) hereafter.

To quantify the optical gain, we use the established concept of material gain $g_i(\lambda, t)$, which is a translation of the excited-state absorbance $A(\lambda, t)$ measured during transient absorption spectroscopy (Methods)[13,19,33,34]. As a time–wavelength-dependent quantity, g_i delivers the three gain parameters discussed earlier: gain lifetime τ_G, threshold n_{th} and material gain coefficient g_i. Figure 1c shows a time–wavelength map of $g_i(\lambda, t)$ measured on 12 nm CdS BNCs for photoexcitation at 400 nm, creating a carrier density $n = \langle N \rangle / V = 5.3 \times 10^{19}$ cm^{-3}, where V is the volume of the nanocrystal and $\langle N \rangle$ is determined from the cross section and photon flux (Methods and Supplementary Section 1.5). For this pair density, g_i exceeds 20,000 cm^{-1} and extends from 465 to ~550 nm, thereby surpassing the bulk bandgap (517 nm). Moreover, $g_i > 0$ persists close to the time limit of our experiment, that is, 3 ns. We proceed to slice the data to obtain the spectra (Fig. 1d,e)

https://doi.org/10.1038/s41565-023-01521-0

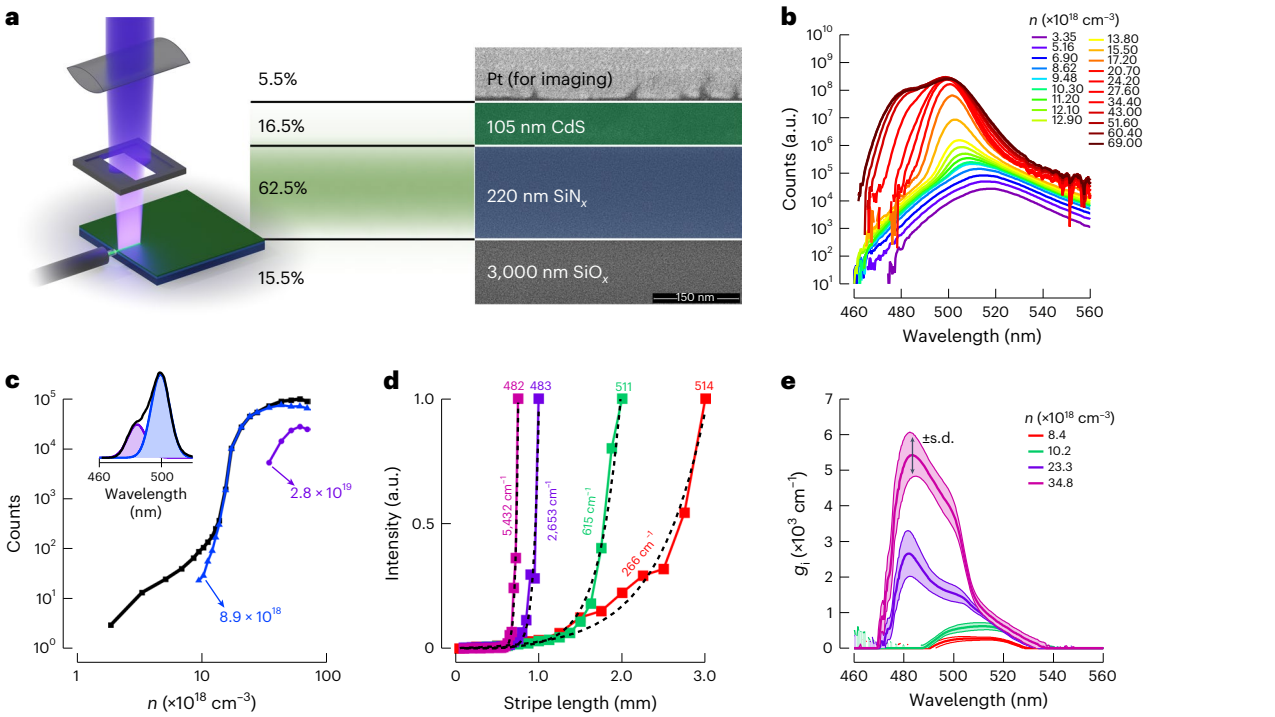

Fig. 2 | ASE in thin-film CdS BNCs. a, Schematic of the ASE setup with stripe illumination pumping and fibre-edge collection. Cross-section and optical-mode (green) calculations of the silicon nitride/BNC stacks used. The percentages indicate the degree of mode confinement in each layer of the stack. **b**, ASE spectra at a fixed stripe length of 3 mm using 400 nm pumping. We observe a strong supra-linear increase and sizable broadening of the collected luminescence to a double-peak structure. **c**, Integrated counts of the total spectrum (black) and the separate ASE$_n$ features (blue and purple), showing a clear threshold behaviour, indicated by the blue and purple arrows. The horizontal axis is expressed as the created carrier density n. **d**, VSL measurements at select different wavelengths (482, 483, 513 and 514 nm) at a fixed pump power, showing a supra-linear increase with increasing amplifier length. The dashed lines indicate fits to extract the modal gain coefficients. **e**, VSL spectrum showing the recalculated intrinsic gain versus wavelength at different carrier densities obtained from combining larger datasets than those shown in **d**. The error bars are defined based on the standard deviation (s.d.) from the exponential growth model for stripe length amplification (Supplementary Section 11).

and dynamics (Fig. 1f) for increasing carrier densities n under varying pump wavelengths.

In Fig. 1d, g_i spectra at 3 ps with 400 nm pumping are shown. A net gain window opens up near the bandgap at $n \approx 10^{18}$ cm^{-3}, only to increase—without any signs of saturation—to nearly 50,000 cm^{-1} at shorter wavelengths. The gain window simultaneously shifts to longer wavelengths, away from the linear absorption, thereby showing a net stimulated emission in the wavelength range from 520 to 600 nm, where linear absorption is absent. Such gain coefficients outperform zero-dimensional systems (<3,000 cm^{-1}) (ref. 19), leaving only CdSe nanoplatelets as the closest second (<20,000 cm^{-1}) (ref. 17). Figure 1e shows the g_i spectra, even after 485 nm pumping. Again, a window of net gain opens up, eventually stretching over a range from 490 to 560 nm. The material gain does saturate across the entire spectrum, peaking at 7,000 cm^{-1}. Figure 1f shows the dynamics of the material gain at the bandgap after 485 nm (top) and 400 nm (bottom) pumping. We observe a net gain up to 2.9 ns, both for resonant (485 nm) and hot (400 nm) excitation. We define this temporal window as the inverted-state (or gain) lifetime $\tau_G = 2.9$ ns. This multi-nanosecond lifetime matches state-of-the-art timescales observed in alloyed shell CdSe/CdS QDs[21] or surface quantum well CdSe/CdS systems[14], both—however—made using more complex synthesis procedures.

From ASE to quasi-CW lasing

Next, ASE is collected from the side of a slab waveguide structure under variable stripe length (VSL) illumination (Fig. 2a). We obtain clear amplification characteristics (Fig. 2b), where the spectrum of the spontaneous emission not only increases supra-linearly but it also narrows down from 25 to 8 nm. At higher pump fluxes, the initial ASE peak saturates and a shoulder at shorter wavelengths grows in. A clear threshold of $n = 8.9(1) \times 10^{18}$ cm^{-3} is identified for the main ASE lobe (Fig. 2c). A higher threshold of $2.8(3) \times 10^{19}$ cm^{-3} characterizes the second high-energy-gain band. Several observations of the ASE with BNCs contrast with the numerous reports on other solution-processable confined QD systems. First, the ASE output builds four orders of magnitude over the spontaneous emission, opposed to a more modest one to two orders for confined QDs[4]. Second, the spectra neither indicate any clear saturation nor any narrow lines typical for discrete two-level systems[35]. By varying the pumped stripe length, we can also quantify the modal gain g_m at every wavelength (Fig. 2d). By using a calculated optical confinement factor Γ (Fig. 2a) and volume fraction f, we can renormalize g_m to a material gain of $g_i = \frac{g_m}{\Gamma f}$ (ref. 36). As such, we obtain the gain spectra (Fig. 2e) that indicate a similar amplification bandwidth of the results (Fig. 1d) in solution. Deviations in the absolute gain magnitude arise from interplays between dynamically evolving spontaneous emission and amplification not encountered in dilute dispersions (Supplementary Section 3.1).

Building on the broadband and efficient ASE, we develop a series of optically pumped, small-footprint photonic crystal (PhC) surface-emitting lasers. These are uniquely out-of-plane-emitting lasers with in-plane feedback[37,38]. Figure 3a shows the PhC structure used, which consists of a second-order two-dimensional in-plane grating etched out of silicon nitride. A thin layer of CdS BNCs is spin coated on top and fills the air gaps. The device is first pumped using 450 nm femtosecond laser pulses. Using a PhC pitch variation between 280 and 305 nm, lasing is obtained from 485 to 522 nm (Fig. 3b (top)). Picking out a few cavities, Fig. 3c (top) shows a varying threshold (Fig. 3d (black)) between 10 and 100 μJ cm^{-2} for varying emission wavelengths (red and blue). Next, the same samples were photoexcited with 7 ns

https://doi.org/10.1038/s41565-023-01521-0

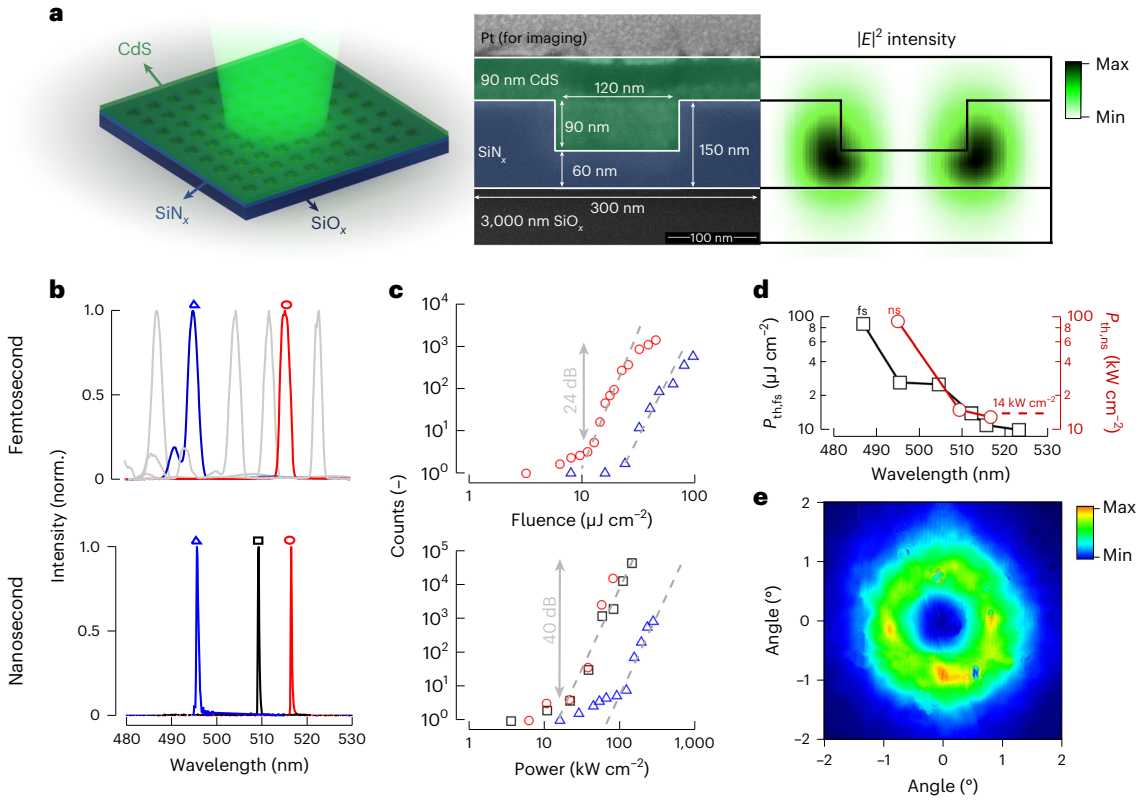

Fig. 3 | Optically pumped lasing. a, Schematic of the PhC surface-emitting lasers consisting of a BNC layer (green) covering a two-dimensional PhC grating etched into silicon nitride grown on silicon oxide (left). The pitch of the PhC array determines the lasing resonance. A scanning electron microscopy cross section together with the simulated mode profile (right) for the electric-field intensity, showing a high confinement in the gaps where BNC filling is obtained. **b**, Normalized collected lasing spectra of cavities with varying pitches using (top) 120 fs at 450 nm pulses and 7 ns at 355 nm pulses (bottom). **c**, Normalized output versus pump fluence for femtosecond and nanosecond scales in cavities with varying pitches in line with the spectra shown in **b**. **d**, Wavelength-dependent threshold is observed under both femtosecond (fs; black squares) and nanosecond (ns; red circles) excitations. **e**, Beam profile of a typical device under femtosecond pumping collected at 1 m distance, translated here into a divergence angle in both spatial directions.

pulses at 355 nm with the same spot size, obtaining a set of quasi-CW lasers emitting from 495 to 518 nm (Fig. 3b (bottom)). The thresholds are as low as 14 kW cm^{-2} (Fig. 3c (bottom)), outcompeting similar reports[39–41]. The 7 ns timescale outpaces the known non-radiative loss in our system, as shown later, making it a quasi-CW operation. Finally, Fig. 3e shows the beam profile collected at 1 m from a typical device under femtosecond excitation. The very small divergence (±1°) and a peculiar ring shape is expected for the geometry of our specific PhC surface-emitting lasers (Supplementary Section 5).

Modelling with strong bandgap renormalization

The bulk optical gain is mediated by a classical state filling of continuous bands dictated by Fermi–Dirac statistics, in terms defined by a carrier temperature T and carrier density n. Hereafter, we assume that the band structure of CdS can be described by a single valence band and a single conduction band, although with different curvatures described by the effective mass (Fig. 4a).

We express the material gain at photon energy E as the product of the linear absorption at E and the occupation factors for conduction f_c and valence bands f_v states (Supplementary Section 5) as

$$g_i(E,n,T) = \mu_{i,0}(E) \times [f_c(E,n,T) - f_v(E,n,T)]. \quad (1)$$

State filling leads to population inversion or $f_v < f_c$ at a given photon energy E. Since we know n, only the carrier temperature T remains unknown. However, T can be extracted from femtosecond photoluminescence (fPL)[42] spectroscopy (Methods and Supplementary Section 6), where one directly obtains T from fitting the fPL spectra[43]:

$$\mathrm{PL}(E) \propto \sqrt{E - E_g} \times e^{-\frac{E-E_g}{k_B T}}. \quad (2)$$

Figure 4b shows a time–wavelength map of the fPL at 400 nm. Taking horizontal slices at 3 ps, we can fit equation (2) to obtain T as a function of time at varying pump powers (Fig. 4c). With the experimental input for both n and T, we model the full gain spectrum using equation (1). Figure 4d shows that the model reproduces the experimental shape, but misses the low-energy-gain window and severely underestimates the gain. To improve the model, we include a spectral redshift based on the experimental observations of sub-bandgap gain, ASE and lasing. In the context of bulk semiconductors, such an energy shift is often referred to as a bandgap renormalization (BGR) Δ_{BGR}, which modifies equation (1) to

$$g_i(E,n,T) = \mu_{i,0}(E - \Delta_{BGR}) \times [f_c(E,n,T) - f_v(E,n,T)]. \quad (3)$$

Using $\Delta_{BGR} = 45$ meV, Fig. 4d (solid black line) now shows a perfect match with the experimental gain spectrum. In fact, using Δ_{BGR} as the only freely adjustable parameter, we can quantitatively reproduce all the experimental g_i spectra (Fig. 4e).

Clearly, the BGR is the main driver for the gain observed in BNCs. Similar to the attractive biexciton interaction in confined QDs, the reduction in the bandgap of BNCs under increasing carrier density leads to an energetic redshift in the excited-state absorption spectrum[11,19]. Despite a similar impact on the spectrum, BGR has a fairly different origin. In strongly confined systems, multi-exciton energetics are the net result of discrete carrier–carrier repulsions[11,14,44] and

https://doi.org/10.1038/s41565-023-01521-0

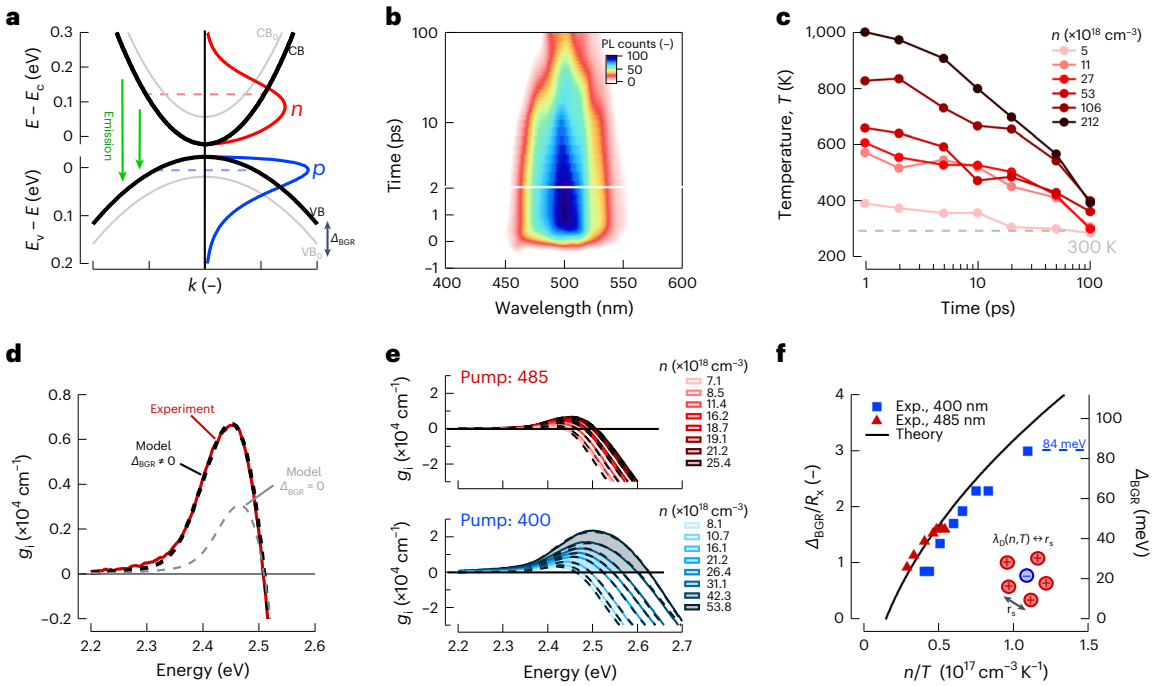

Fig. 4 | Quantitative bulk gain model. a, A single valence band (VB) and conduction band (CB; grey) are shown, together with the calculated electron (red; n) and hole (blue; p) densities. The black bands refer to the renormalized gap. The green arrows indicate a radiative recombination through stimulated emission. **b**, Two-dimensional time–wavelength map of transient PL after photoexcitation with 400 nm. **c**, Carrier temperature T for different time delays and select carrier densities (Supplementary Section 8). The horizontal dashed line refers to room temperature (300 K). **d**, Material gain spectrum (dashed grey) with $n = 1.8 \times 10^{19}$ cm^{-3} and $T = 440$ K without BGR. The dashed black line adds a BGR of 45 meV. The solid red line indicates the experimental data. **e**, Correspondence is found between experiment (solid) and model (dashed) using only Δ_{BGR} as a freely adjustable parameter for both 485 nm (top) and 400 nm (bottom) pumping. **f**, Obtained Δ_{BGR} values, both absolute (right axis) and normalized to the bulk-exciton binding energy of wz–CdS $R_X = 28$ meV (left axis), from full-spectrum fits for an increasing carrier density in the case of 400 and 485 nm pumping. The solid black line is a parameter-free theoretical prediction. The Δ_{BGR} value reaches 84 meV without clear signs of saturation. The inset shows a cartoon with a sea of holes (red circles) screening a single electron (blue circle) that sketches the physical concept leading to the BGR effect, where r_s is the interparticle separation and λ_D is the Debye screening length depending on temperature T and carrier density n.

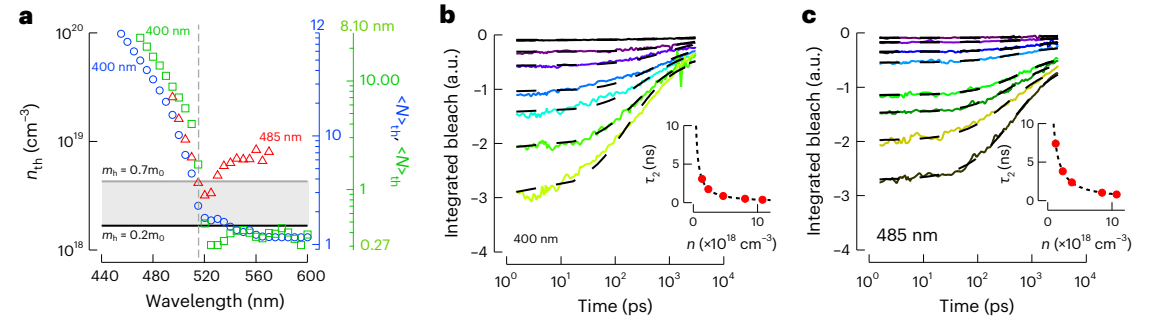

Fig. 5 | Gain threshold and dynamics of CdS BNCs. a, Minimum carrier density required to reach transparency $g_i = 0$, called the threshold density n_{th}, as a function of wavelength for the 12 nm BNCs. The green square markers show the result for the 8.1 nm BNCs. The pump wavelengths are indicated (400 or 485 nm). The vertical axes on the right indicate the same densities reported as the absolute number of electron–hole pairs $\langle N \rangle$ per BNC. The horizontal lines indicate the theoretically predicted threshold range using a range for the hole effective masses $m_{LH,HH}$. **b**,**c**, Recombination dynamics of charge carriers in CdS BNCs tracked by the integrated bleach around the bandgap region (420–600 nm; coloured traces) for 400 nm (**b**) and 485 nm (**c**) pumping. Global fits using a mixed first- and second-order recombination model are indicated by the dashed black lines. The insets show the predicted two-body lifetime $\tau_2 = 1/k_2 n_0$ (red dots) in nanoseconds for various excitation densities, where n_0 is the initial charge density and k_2 is the second-order recombination constant obtained from the global fit. The dashed grey line is a guide to the eye.

attractions; the BGR shift in bulk semiconductors is described as a self-energy correction of individual charge carriers due to increased screening in the plasma formed at a high carrier density[45]. Typically, such stabilizing effects become important in a regime beyond the so-called Mott density, which is reached when the interparticle separation $r_s \propto n^{-1/3}$ reaches the Debye screening length λ_D. The latter is dependent on the carrier plasma's temperature T and carrier density n, resulting in an overall expression of the BGR effect depending on both parameters. Note that these effects are totally and purely electronic in origin. The lattice in polar semiconductors barely heats up despite the high carrier gas temperatures due to the massive discrepancy in heat capacity between both. To the best of our knowledge, sizable BGR effects have not been reported yet in solution-processable materials; yet, BGR clearly proves to be of extreme value. Indeed, BGR shifts the

window of stimulated emission away from linear absorption, effectively bringing larger-oscillator-strength higher-energy transitions towards the bandgap. Similar spectral redshifting was already shown to be beneficial for strongly confined CdSe/CdS QDs; yet, the largest BGR shifts observed here (84 meV) in BNCs exceed typical biexciton redshifts (<10 meV) observed in confined systems by an order of magnitude[4,19].

Following other works[45,46], the BGR in three-dimensional semiconductors under the assumption of static screening is given as

$$\frac{\Delta_{BGR}}{R_X} = \left(\frac{n}{n_M(T)}\right)^{1/2} - 2 = \alpha^{-1/2}\left(\frac{n}{T}\right)^{1/2} - 2, \quad (4)$$

where T is the carrier gas temperature, n_M is the Mott density (Supplementary Section 8) and $R_X = 28$ meV is the bulk-exciton binding energy of wz–CdS (ref. 47). Figure 4f shows the excellent theoretical prediction of Δ_{BGR} together with the experimental Δ_{BGR} values, where the latter are obtained from best fits to the material gain spectra.

Figure 5a summarizes the threshold densities n_{th} required for transparency ($g_i = 0$) for the 8.1 and 12.0 nm BNCs, showing that the lowest density required to achieve transparency is 3×10^{18} cm^{-3} and occurs at (and below) the bandgap. We observe an increase in n_{th} towards shorter wavelengths. At longer wavelengths, the 400 nm pump produces a sizably lower gain threshold opposed to the 485 nm case. The lowest value for n_{th} corresponds to $n_{th} = 1.1 \times 10^{18}$ cm^{-3}, equivalent to a single electron–hole pair on average, $\langle N \rangle = 1$, for the 12.0 nm BNCs. Remarkably however, the 8.1 nm BNCs show a similar n_{th}, which implies that $\langle N \rangle = 0.27 < 1$ is the absolute number per nanocrystal required for optical gain. Within a bulk picture, one can analytically calculate the threshold in the absence of spectral shifts (Supplementary Section 5)[48]. We find a good correspondence with the experimental thresholds (the horizontal lines in Fig. 5a indicate varying hole masses).

To understand the nanosecond gain lifetime, we have to focus on the recombination dynamics of the charge carriers. Again, using the notion of bulk photophysics, these dynamics can be described using the following general rate equation:

$$-\frac{dn}{dt} = k_1 n + k_2 n^2 + k_3 n^3 \approx k_1 n + k_2 n^2, \quad (5)$$

where each rate k_i relates to a specific physical process. In the bulk view where excitons are considered to be absent beyond the Mott density, we take n (p) as the unbound electron (hole) density. In this case, k_1 refers to a linear charge-trapping mechanism. The second-order recombination constant k_2 relates to radiative electron–hole pair recombination. One can assign a density-dependent lifetime to the two-body recombination process using the initial carrier density n_0: $\tau_2 = \frac{1}{k_2 n_0}$. Finally, k_3 relates to non-radiative Auger recombination. The lifetime associated with Auger processes can be written as $\tau_{Auger} = \frac{1}{k_3 n_0^2}$ (ref. 49). To deal with the various orders, we assume that trapping is fluence independent and fix $k_1 = 0.33$ ns^{-1} to the value obtained from the PL decay analysis above. At the carrier densities used in this work, the Auger timescale in bulk CdS is 0.1–1.0 µs, far slower than our time window[49]. This allows us to ignore the cubic term in equation (5), leaving a mixed first- and second-order process whose fitting results in well-defined k_2 values. Using the fact that the radiative k_2 process is the limiting factor for sustaining a net optical gain, we can estimate the gain lifetime τ_G as the time it takes to annihilate n_{th}, as determined above:

$$\tau_{G,485} = \frac{1}{k_{2,485} n_{th}} = 2.9 \text{ ns}. \quad (6)$$

This estimation matches the observed τ_G of 3 ns. It also coincidentally lines up with the trapping rate k_1 for single charge carriers as extracted from the PL decay.

The remarkable observations of the ASE experiments line up with our BNCs behaving as bulk-like semiconductors. In such systems with a high density of states, we can, in fact, maintain state filling in closely spaced energy levels to obtain a net gain over a continuous and broad energy range. The second important observation was the high dynamic range. We can understand this since the limiting process is radiative recombination (k_2), which only speeds up light emission at a higher density, outcompeting any unwanted trapping and Auger processes. Furthermore, the lower-limit threshold for quasi-CW lasing can be approximated from the estimate $P_{th,fs}/\tau_G$ resulting in ~5 kW cm^{-2}. The nanosecond thresholds are in line with this estimate, which confirms our coherent understanding of the BNCs as gain materials.

Conclusions

Low-threshold broadband ASE and quasi-CW lasing were demonstrated using CdS BNCs. The gain metrics coherently transpire into lasing devices and can be quantitatively explained using a bulk photophysics model combined with a large BGR, an effect unobserved in solution-processable materials to date, to the best of our knowledge. Our results are promising for efficient solution-processable gain materials capable of operating under realistic operating conditions, such as CW optical and d.c. electrical pumping. In addition, they also provide a revival of the benefits of bulk photophysics such as a high and continuous density of states combined with large cross sections and limited non-radiative losses. Due to historical limitations in material quality and an inability to confine both light and carriers in a printable material with bulk optical properties, these effects were never fully exploited (Supplementary Section 11). A possible downside of the bulk is the limited spectral tuning, but this can be remedied by alloying[50,51]. Our findings encourage a revision of the potential for bulk photophysics in optoelectronics in general.

Online content

Any methods, additional references, Nature Portfolio reporting summaries, source data, extended data, supplementary information, acknowledgements, peer review information; details of author contributions and competing interests; and statements of data and code availability are available at https://doi.org/10.1038/s41565-023-01521-0.

References

1. Zhang, Q., Tao, W., Huang, J., Xia, R. & Cabanillas-Gonzalez, J. Toward electrically pumped organic lasers: a review and outlook on material developments and resonator architectures. *Adv. Photon. Res.* **2**, 2000155 (2021).
2. Park, Y.-S., Roh, J., Diroll, B. T., Schaller, R. D. & Klimov, V. I. Colloidal quantum dot lasers. *Nat. Rev. Mater.* **6**, 382–401 (2021).
3. Geiregat, P., Van Thourhout, D. & Hens, Z. A bright future for colloidal quantum dot lasers. *npg Asia Mater.* **11**, 41 (2019).
4. Pietryga, M. et al. Spectroscopic and device aspects of nanocrystal quantum dots. *Chem. Rev.* **116**, 10513–10622 (2016).
5. Shirasaki, Y., Supran, G. J., Bawendi, M. G. & Bulović, V. Emergence of colloidal quantum-dot light-emitting technologies. *Nat. Photon.* **7**, 13–23 (2012).
6. Semonin, O. E. et al. Peak external photocurrent quantum efficiency exceeding 100% via MEG in a quantum dot solar cell. *Science* **334**, 1530–1533 (2011).
7. Deng, Z., Jeong, K. S. & Guyot-Sionnest, P. Colloidal quantum dots intraband photodetectors. *ACS Nano* **8**, 11707–11714 (2014).
8. Livache, C., Martinez, B., Goubet, N., Ramade, J. & Lhuillier, E. Road map for nanocrystal based infrared photodetectors. *Front. Chem.* **6**, 575 (2018).
9. Garcia de Arquer, F. P., Armin, A., Meredith, P. & Sargent, E. Solution-processed semiconductors for next-generation photo-detectors. *Nat. Rev. Mater.* **2**, 16100 (2017).

10. Klimov, V. I. et al. Optical gain and stimulated emission in nanocrystal quantum dots. *Science* **290**, 314–317 (2000).
11. Klimov, V. I. et al. Single-exciton optical gain in semiconductor nanocrystals. *Nature* **447**, 441–446 (2007).
12. Wu, K., Park, Y.-S., Lim, J. & Klimov, V. I. Towards zero-threshold optical gain using charged semiconductor quantum dots. *Nat. Nanotechnol.* **12**, 1140–1147 (2017).
13. Geiregat, P. et al. Continuous-wave infrared optical gain and amplified spontaneous emission at ultralow threshold by colloidal HgTe quantum dots. *Nat. Mater.* **17**, 35–42 (2017).
14. Cassidy, J. et al. Quantum shells boost the optical gain of lasing media. *ACS Nano* **16**, 3017–3026 (2022).
15. Ithurria, S. et al. Colloidal nanoplatelets with two-dimensional electronic structure. *Nat. Mater.* **10**, 936–941 (2011).
16. Guzelturk, B., Pelton, M., Olutas, M. & Demir, H. V. Giant modal gain coefficients in colloidal II-VI nanoplatelets. *Nano Lett.* **19**, 277–282 (2018).
17. Geiregat, P. et al. Thermodynamic equilibrium between excitons and excitonic molecules dictates optical gain in colloidal CdSe quantum wells. *J. Phys. Chem. Lett.* **10**, 3637–3644 (2019).
18. Li, Q., Liu, Q., Schaller, R. D. & Lian, T. Reducing the optical gain threshold in two-dimensional CdSe nanoplatelets by the giant oscillator strength transition effect. *J. Phys. Chem. Lett.* **10**, 1624–1632 (2019).
19. Bisschop, S., Geiregat, P., Aubert, T. & Hens, Z. The impact of core/shell sizes on the optical gain characteristics of CdSe/CdS quantum dots. *ACS Nano* **12**, 9011–9021 (2018).
20. Fan, F. et al. Continuous-wave lasing in colloical quantum dot solids enabled by facet-selective epitaxy. *Nature* **544**, 75–79 (2017).
21. Lim, J., Park, Y.-S. & Klimov, V. I. Optical gain in colloidal quantum dots achieved with direct-current electrical pumping. *Nat. Mater.* **17**, 42–49 (2017).
22. Yang, Z., Pelton, M., Fedin, I. & Talapin, D. V. A room temperature continuous-wave nanolaser using colloidal quantum wells. *Nat. Commun.* **8**, 143 (2017).
23. Xie, W. et al. On-chip integrated quantum-dot silicon-nitride microdisk lasers. *Adv. Mater.* **29**, 1604866 (2017).
24. Xie, W. et al. Colloidal quantum dots enabling coherent light sources for integrated silicon-nitride photonics. *IEEE J. Sel. Topics Quantum Electron.* **23**, 8200913 (2017).
25. Jung, H. et al. Two-band optical gain and ultrabright electroluminescence from colloidal quantum dots at 1,000 A cm^{-2}. *Nat. Commun.* **13**, 3734 (2022).
26. Ahn, N. et al. Electrically driven amplified spontaneous emission from colloidal quantum dots. *Nature* **617**, 79–85 (2023).
27. Chernikov, A., Ruppert, C., Hill, H. M., Rigosi, A. F. & Heinz, T. F. Population inversion and giant bandgap renormalization in atomically thin WS_2 layers. *Nat. Photon.* **9**, 466–470 (2015).
28. Hens, Z. & Moreels, I. Light absorption by colloidal semiconductor quantum dots. *J. Mater. Chem.* **22**, 10406 (2012).
29. Ghobadi, N. Band gap determination using absorption spectrum fitting procedure. *Int. Nano Lett.* **3**, 2 (2013).
30. Maes, J. et al. Size and concentration determination of colloidal nanocrystals by small-angle X-ray scattering. *Chem. Mater.* **30**, 3952–3962 (2018).
31. Thambidurai, M. et al. Strong quantum confinement effect in nanocrystalline CdS. *J. Mater. Sci.* **45**, 3254–3258 (2010).
32. Aubert, T. et al. General expression for the size-dependent optical properties of quantum dots. *Nano Lett.* **22**, 1778–1785 (2022).
33. Geiregat, P. et al. Using bulk-like nanocrystals to probe intrinsic optical gain characteristics of inorganic lead halide perovskites. *ACS Nano* **12**, 10178–10188 (2018).
34. Rodà, C. et al. Stimulated emission through an electron-hole plasma in colloidal CdSe quantum rings. *Nano Lett.* **21**, 10062–10069 (2021).
35. Di Stasio, F., Polovitsyn, A., Angeloni, I., Moreels, I. & Krahne, R. Broadband amplified spontaneous emission and random lasing from wurtzite CdSe/CdS 'giant-shell' nanocrystals. *ACS Photon.* **3**, 2083–2088 (2016).
36. Aellen, M. & Norris, D. J. Understanding optical gain: which confinement factor is correct? *ACS Photon.* **9**, 3498–3505 (2022).
37. Hirose, K. et al. Watt-class high-power, high-beam-quality photonic-crystal lasers. *Nat. Photon.* **8**, 406–411 (2014).
38. Sakata, R. et al. Photonic-crystal surface-emitting lasers with modulated photonic crystals enabling 2D beam scanning and various beam pattern emission. *Appl. Phys. Lett.* **122**, 130503 (2023).
39. Pinchetti, V. et al. Effect of core/shell interface on carrier dynamics and optical gain properties of dual-color emitting CdSe/CdS nanocrystals. *ACS Nano* **10**, 6877–6887 (2016).
40. Zhu, Y. et al. On-chip single-mode distributed feedback colloidal quantum dot laser under nanosecond pumping. *ACS Photon.* **4**, 2446–2452 (2017).
41. Adachi, M. M. et al. Microsecond-sustained lasing from colloidal quantum dot solids. *Nat. Commun.* **6**, 8694 (2015).
42. Chen, K., Gallaher, J. K., Barker, A. J. & Hodgkiss, J. M. Transient grating photoluminescence spectroscopy: an ultrafast method of gating broadband spectra. *J. Phys. Chem. Lett.* **5**, 1732–1737 (2014).
43. Pelant, I. & Valenta, J. *Luminescence Spectroscopy of Semiconductors* (Oxford Univ. Press, 2012).
44. Geiregat, P. et al. Coulomb shifts upon exciton addition to photoexcited PbS colloidal quantum dots. *J. Phys. Chem. C* **118**, 22284–22290 (2014).
45. Dneprovskii, V. S., Klimov, V. I. & Novikov, M. G. Dynamics and mechanisms of recombination of electron-hole plasma and high-density excitons in CdS and CdSe. *Sov. Phys. JETP* **3**, 468–478 (1991).
46. Tränkle, B. et al. Dimensionality dependence of the band-gap renomalization in two- and three dimensional electron-hole plasmas. *Phys. Rev. Lett.* **58**, 419 (1987).
47. Saito, H. & Göbel, E. Picosecond spectroscopy of highly excited Cds. *Phys. Rev. B* **31**, 2360–2369 (1985).
48. Asano, K. & Yoshioka, T. Exciton-Mott physics in two-dimensional electron-hole systems: phase diagram and single-particle spectra. *J. Phys. Soc. Jpn* **82**, 084702 (2014).
49. Melnychuk, C. & Guyot-Sionnest, P. Multicarrier dynamics in quantum dots. *Chem. Rev.* **121**, 2325–2372 (2021).
50. Aubert, T. et al. Homogeneously alloyed CdSeS quantum dots: an efficient synthesis for full optical tunability. *Chem. Mater.* **25**, 2388–2390 (2013).
51. Liu, Y. K. et al. Wavelength-tunable lasing in single-crystal $CdS_{1-x}Se_x$ nanoribbons. *Nanotechnology* **18**, 365606 (2007).

Methods

Materials and precursors

Anhydrous cadmium oxide (99.5%) was purchased from Chemlab Analytical, sulfur powder (S, 99.5%) was purchased from Sigma-Aldrich and tri-octylphosphine (TOP, min. 97.0%) was purchased from Strem Chemicals. 1-Octadecene (ODE, tech. 90%) and oleic acid (tech. 90%) were purchased from Alfa Aesar and further purified. A cadmium oleate (0.5 M) solution is prepared as follows: 1,024 g cadmium oxide powder (8 mmol), 8 ml oleic acid and 8 ml anhydrous ODE were added into a 50 ml three-necked flask. The mixture was then heated up to 105 °C under a vacuum and maintained for 60 min. Next, the flask was heated to 300 °C under a N_2 flow and kept for 5 min at that temperature. A transparent product forms and the obtained cadmium oleate solution (0.5 M) was cooled to room temperature and stored in a N_2 atmosphere. Since the solution solidifies, it should be gently heated before use. A TOPS (0.5 M) solution is prepared as follows. In a 20 ml vial, 10 ml of TOP was added to 0.160 g of elemental S powder (5 mmol) and the solution was stirred at 90 °C for 30 min under N_2 gas until fully complexed. All the stock solutions were stored in sealed 20 ml vials under a N_2 atmosphere.

Synthesis protocol

In a 50 ml three-necked round-bottom flask, 8 ml anhydrous ODE was loaded and heated to 105 °C under a vacuum and kept for 60 min. Then, the flask was filled with N_2 and heated to 325 °C. An equimolar solution of preheated cadmium oleate and TOPS was mixed and slowly injected into the ODE at the rate of 2 ml h^{-1}. The injection time was adjusted to synthesize CdS BNCs of different sizes. For example, to synthesize monodisperse 12 nm CdS BNCs, 0.75 ml of cadmium oleate and 0.75 ml of TOPS solutions were mixed together and injected for 45 min. After the injection was complete, the solution was left undisturbed at 325 °C for 15 min for the remaining precursors to fully react and to allow ripening of any smaller particles. Afterwards, the particles were purified twice using a 1:3 ratio mix of methanol and 2-propanol and later redispersed in toluene. To obtain the 8 nm particles, an aliquot was taken at the 70 min mark and size-selective precipitation was used to remove any remaining smaller particles.

Transient absorption spectroscopy

Samples were excited using 110 fs pump pulses at 400 nm through second-harmonic generation in α-BBO, or at 480 nm created from the 800 nm fundamental (Spitfire Ace, Spectra Physics) through nonlinear conversion in an optical parametric amplifier (TOPAS, Light Conversion). The probe pulses were generated in a 1-mm-thick CaF_2 crystal using the 800 nm fundamental. The pulses were delayed relative to the pump using a delay stage with the maximum delay of 6.0 ns for 485 nm pumping and 3.3 ns for 400 nm pumping. The probe spectrum in our experiments covers the ultraviolet–visible window from 420 to 700 nm. CdS BNCs were dispersed in an optically transparent solvent (toluene) and continuously stirred to avoid charging or photodegradation. The pump wavelength and sample concentration were chosen to obtain an optimal trade-off between having a good signal at the band-edge transitions and still not having too strong absorption at the pump wavelength to assure uniform pumping of the sample.

The average number of absorbed photons (or equivalently created excitons) at time zero, noted as $\langle N \rangle$, can be calculated from photon flux J_{ph}, cuvette length L and nanocrystal absorption cross section at the pump wavelength σ_{λ_p}: $\langle N \rangle = J_{ph} \times \sigma_{\lambda_p} \times \frac{1-e^{-\alpha_{0,\lambda_p} L}}{\alpha_{0,\lambda_p} L}$ (Supplementary Section 1). The photon flux is calculated from the beam area, obtained through a Thorlabs charge-coupled device beam profiler, and defined as $A_{beam} = 2\pi \times \sigma_x \sigma_y$, where σ_i is the standard deviation in the $i = x$ or y direction.

The absorption cross section of the BNCs can be calculated as $\sigma = \mu_{i,0} \times V_{QD}$ (Supplementary Section 1.3). Based on this, we can translate the photon flux into an average number of absorbed electron–hole pairs per nanocrystal, $\langle N \rangle = J_{ph} \times \sigma$. More useful in the case of bulk semiconductors is the notion of a mean charge density $n = \langle N \rangle / V_{QD}$. For example, a single electron–hole pair $\langle N \rangle = 1$ in an 8.1 nm QD corresponds to a carrier density of $n = 3.6 \times 10^{18}$ cm^{-3}. The decreasing absorption cross section at 485 nm under increased pumping is taken into account as $\sigma_{485} = \sigma_{485}(n = 0) \times \frac{A_{485}(n)}{A_{485}(n=0)}$, where $A(n)$ is evaluated at 0.5 ps.

Quantifying spectroscopy

Quantifying and modelling the optical gain relies on studying the time–wavelength window, where absorbance A of the material at hand turns negative ($A < 0$) at a given carrier density. The latter can be calculated based on the volume of the crystals and the absorbed photon density (Methods). The former can be easily set up using a transient absorption experiment since $A(\lambda, t) = \Delta A(\lambda, t) + A_0(\lambda)$, where ΔA is the differential absorbance. Since A still depends on concentration and path length, we again normalize it to the intrinsic coefficient $\mu_i(\lambda, t)$ (ref. 28). Since we are interested in the net optical gain, we define the material gain $g_i(\lambda, t) = -\mu_i(\lambda, t)$. Using this quantity, we can directly compare the results with other reports in the literature[16,19,33] and also obtain modal gain coefficients g_m, that is, those experienced by a confined photonic mode in a laser cavity, as shown later. Here $g_i(\lambda, t)$ is a time- and wavelength-dependent quantity, which contains all the relevant gain metrics of the material such as (1) the threshold $n_{th}(\lambda)$, minimum carrier density to obtain $g_i(\lambda, t) > 0$; (2) the magnitude and spectral width $g_i(\lambda, t_0)$, obtained from similar spectral slicing at fixed delays; and (3) the lifetime $\tau_G(\lambda)$, that is, the time window for which $g_i(\lambda)$ remains positive.

fPL spectroscopy

For the detection of broadband PL transients on a sub-picosecond timescale, we used the transient grating PL technique[42]. The output of a femtosecond Ti:S laser was split into the pump and gate parts. For the pump part, second-harmonic (400 nm) generation was used in the experiments and focused onto a 50 μm^2 spot onto the sample. During the measurement, the sample was continuously stirred in a 1 mm cuvette to avoid photoinduced degradation effects or charging of the nanoparticles. The PL signal from the sample was collected and refocused onto the gate medium—a 1 mm fused silica crystal—using a pair of off-axis parabolic mirrors. For the gate part, about 40 μJ of the 800 nm output was split using a 50/50 beamsplitter to generate the two gate beams and focused onto the gate medium at a crossing angle of approximately 8° and overlapped with the PL in a boxcar geometry. The two gate beams, which spatially and temporally overlap inside the gate medium, generate a laser-induced grating. This transient grating acts like an ultrafast optical shutter to temporally resolve the broadband PL signals by diffracting the gated signal from the PL background. Two achromatic lenses collimated and focused the gated signals onto the spectrometer entrance (Princeton Instruments SP-2300), and the gated PL spectra were measured by an intensified charge-coupled device camera (Princeton Instruments, PIMAX3). A 435 nm long-pass filter and 750 nm short-pass filter were used to remove the residual pump and intense 800 nm gate, respectively. The time delay between the pump and gate beams was controlled via a motorized optical delay line. For each transient PL spectrum, 30,000 shots for the time delay at each gate were accumulated. Four sequential scans were conducted and their results were averaged.

ASE/VSL

Samples were spin coated from toluene on ~200-nm-thick silicon nitride deposited by chemical vapour deposition on oxide-on-silicon substrates. By including a high-index layer ($n_{SiNx} = 1.85$), we can increase the mode confinement and hence the net modal gain obtainable. For photoexcitation under femtosecond conditions, a cylindrical lens

was used to create a stripe pattern of the 400 nm, 120 fs excitation source, at 1 kHz.

Optically pumped lasers

All the laser device measurements were carried out at room temperature under ambient conditions, without the use of a cryostat or substrate temperature controller. For laser operation under femtosecond optical pumping, an excitation wavelength of 450 nm is obtained from a 1 kHz pulsed laser system producing 120 fs pulses (Spectra Physics Spitfire combined with Light Conversion TOPAS). For laser operation under nanosecond excitation, 7 ns pump pulses at 355 nm from a Nd:YAG nanosecond pulsed laser (Ekspla, 355 nm; repetition rate, 100 Hz) were focused on the sample. In both cases, the pump was focused on the sample to create a 200 × 200 μm^2 area and the emitted light is confocally collected after passing through an appropriate dichroic mirror to block the pump from reaching the spectrometer.

Reporting summary

Further information on research design is available in the Nature Portfolio Reporting Summary linked to this article.

Data availability

The datasets are available from the corresponding author upon reasonable request.

Acknowledgements

I.T. acknowledges support from FWO-Vlaanderen, grant no. 1S96819N. Z.H., P.G. and M.S. acknowledge funding from the Research Foundation—Flanders (FWO-Vlaanderen) under the SBO PROCEED project (no. S0002019N). Z.H. acknowledges Ghent University for funding (BOF-GOA 01G01019 MANAWORK, FWO Project G0B2921N). D.V.T. acknowledges funding through FWO (G0B2921N). I.W., J.H. and K.C. acknowledge support from the Marsden Fast-Start Fund by the Royal Society of New Zealand through contract VUW1715. I.M., P.G. and S.A.C. acknowledge funding from the Research Foundation—Flanders (FWO-Vlaanderen under grant no. G037221N—HITEC). The TEM measurements were performed at the UGent TEM Core Facility and the spectroscopic measurements at the UGent NoLIMITS Core Facility.

Author contributions

I.T. measured the transient absorption data; developed the modelling framework; fabricated and measured the chips for the ASE, VSL and laser measurements; and analysed the data. M.S. and A.H.K. developed the CdS nanocrystal synthesis and carried out the structural characterization. I.W. and K.C. performed the transient PL measurements. S.A.C. fabricated the CdS thin films for the ASE, VSL and lasing experiments. K.C., J.H., I.M., D.V.T., Z.H. and P.G. were involved to analyse and discuss the results and supervise the research. P.G. wrote the manuscript together with I.T.

Competing interests

The authors declare no competing interests.

Additional information

Supplementary information The online version contains supplementary material available at https://doi.org/10.1038/s41565-023-01521-0.

Correspondence and requests for materials should be addressed to Pieter Geiregat.

Peer review information *Nature Nanotechnology* thanks Sergio Brovelli and the other, anonymous, reviewers for their contribution to the peer review of this work.

nature research

Corresponding author(s): Pieter Geiregat

Lasing Reporting Summary

Nature Research wishes to improve the reproducibility of the work that we publish. This form is intended for publication with all accepted papers reporting claims of lasing and provides structure for consistency and transparency in reporting. Some list items might not apply to an individual manuscript, but all fields must be completed for clarity.

For further information on Nature Research policies, including our data availability policy, see Authors & Referees.

Experimental design

Please check: are the following details reported in the manuscript?

1. Threshold

Plots of device output power versus pump power over a wide range of values indicating a clear threshold	☒ Yes ☐ No	Figure 3 of main text & Figure S7 Supporting Information.

2. Linewidth narrowing

Plots of spectral power density for the emission at pump powers below, around, and above the lasing threshold, indicating a clear linewidth narrowing at threshold	☒ Yes ☐ No	Section sS4-S6 of the Supporting Information, in particular Figure S7, S11 and S12.
Resolution of the spectrometer used to make spectral measurements	☒ Yes ☐ No	Section S6 of the Supporting Information, in particular paragraph on line narrowing experiments.

3. Coherent emission

Measurements of the coherence and/or polarization of the emission	☐ Yes ☒ No	Laser characterization is done using short pulsed excitation for which the actual resulting coherence is (a) typically not well defined and (b) not trivial to collect.

4. Beam spatial profile

Image and/or measurement of the spatial shape and profile of the emission, showing a well-defined beam above threshold	☒ Yes ☐ No	Figure 3e shows a measurement of the near field beam profile, showing a beam with a predictable donut shape and a few degree divergence angle, in - line with modeling of the 2D feedback grating, as described in Section S5.

5. Operating conditions

Description of the laser and pumping conditions *Continuous-wave, pulsed, temperature of operation*	☒ Yes ☐ No	In the main text - methods - and Supporting Information section S4. Everything, from fabrication to measurement, is at room temperature in ambient air, no special precautions were taken in that regard. Measurements were performed both under femtosecond and nanosecond excitation, as shown in Figure 3 of the main text.
Threshold values provided as density values (e.g. W cm^{-2} or J cm^{-2}) taking into account the area of the device	☒ Yes ☐ No	Reported as energy density, microjoules/cm^2 for femtosecond experiments and as a power kW/cm^2 for nanosecond experiments. Also as absorbed photon density in the material (cm^-3) where relevant for the physical model. Device area is dictated by the pump spot in the 2D PhC grating.

6. Alternative explanations

Reasoning as to why alternative explanations have been ruled out as responsible for the emission characteristics *e.g. amplified spontaneous, directional scattering; modification of fluorescence spectrum by the cavity*	☒ Yes ☐ No	The lasing is discussed in detail in the main text and in Supporting Information S4,S5 and S6. In particular ASE is ruled out as it is measured separately (Figure 2 main text) and shows extremely different spectral characteristics, as shown in Figure S12, and in comparison with Figure 3 of the main paper text. Modification of the PL spectrum is not observed below threshold due to the specific nature of the cavity, as explained in section S4 of the Supporting. A very high degree of control is attained over the optical modes as shown in the main text by varying the pitch of the grating leading to well-defined and predictable spectral lines (Figure 3b). Moreover, also the emission pattern can be explained from theory and presents a well-defined out -of-plane nearly collimated beam of light, strongly opposing scattering. Note that also the grating pitch can be correlated 1:1 to the lasing mode wavelength as shown in Figure 3b of the main paper.

7. Theoretical analysis

Theoretical analysis that ensures that the experimental values measured are realistic and reasonable *e.g. laser threshold, linewidth, cavity gain-loss, efficiency*	☒ Yes ☐ No	Laser thresholds are in-line with the fluency needed for net ASE in films and population inversion (lifetime) in solution. The material gain supplied by the BNCs is also large enough at these fluences to overcome the cavity loss, as estimated in Section S4 via the Q-factor of the cavities, see Figure S7. Efficiency is hard to define (or even measure) under pulsed excitation as the collection setup has not been optimized for absolute, deterministic measurements.

8. Statistics

Number of devices fabricated and tested	☒ Yes ☐ No	As shown in Figure 3b of the paper, on a same substrate lasers of different emission wavelengths can be made by varying the pitch on that same substrate, thereby showing great control over the device fabrication. In total, 5 separate layer stacks were built independently and lasing action was obtained every time with only minor variations in laser wavelength due to small fluctuations in layer thicknesses (silicon nitride, BNC film). Combining this with pitch variations with every separate fabrication run, up to 25 separate laser structures were tested and all ran successfully.
Statistical analysis of the device performance and lifetime (time to failure)	☒ Yes ☐ No	Devices are stable under 1 kHz pulsed excitation in ambient at room temperature for up to 1 million laser pulses. This is indicated in Figure S14 in the Supporting Information.